Pergamon

Int. J. Heat Mass Transfer. Vol. 38, No. 4, pp. 665–677, 1995

0017–9310/95 $9.50+0.00

0017–9310(94)00192–8

Simultaneously developing mixed convection in radially rotating rectangular ducts

W. M. YAN

Department of Mechanical Engineering, Hua Fan College of Humanities and Technology, Shi-Ting, Taipei, Taiwan 22305, R.O.C.

and

C. Y. SOONG

Department of Aeronautical Engineering, Chung Cheng Institute of Technology, Taoyuan, Taiwan 33509, R.O.C.

(*Received* 15 *January* 1994 *and in final form* 13 *June* 1994)

Abstract—The present work is concerned with a numerical study on laminar mixed convection flow and heat transfer in the entrance region of rotating isothermal rectangular ducts. The emphasis is placed on the rotational effects, including both the Coriolis force and centrifugal buoyancy, on non-isothermal flow and related heat transfer. The numerical results are presented for air flow in rectangular ducts over a wide range of the parameters. By examining the local field-solutions, the mechanisms for influences of Coriolis and centrifugal buoyancy forces can be addressed in detail. The results reveal that the variations of the local friction factor and heat transfer rate are closely related to the emergence, disappearance, growth, and decay of the rotation-induced secondary vortices. The friction factor and heat transfer rate can be enhanced by Coriolis effect. The predictions also demonstrate that the centrifugal buoyancy presents remarkable effects on the axial evolution of secondary vortices and, therefore, on the flow and heat transfer characteristics in a radially rotating duct. The buoyancy effects are different on the trailing, leading and side walls; and the rotational effects can be altered with the change in cross-sectional aspect-ratio.

INTRODUCTION

Rotating coolant passages are used extensively in rotary machinery as a cooling device for protection of the elements exposed in a high temperature environment, e.g. rotor blades in a turbo-engine. Radially rotating channels are most commonly used where flow and heat transfer mechanisms are very complicated due to the presence of Coriolis-induced secondary flow and rotation-induced buoyancy effects. The former enhances the heat exchange between channel walls and the coolant, and thus is beneficial in cooling efficiency. However, the latter provides an adverse or advantageous effect on heat transfer depending on the heating conditions and the direction of coolant flow.

A vast amount of studies, both theoretical and experimental, exist in the literature for flow and heat transfer characteristics in rotating channels, as is evident in the monograph [1] and recent studies [2, 3]. Only those relevant to the present work are briefly reviewed here. The effects of the Coriolis force on the flow structure in unheated ducts have been examined in a number of the earlier investigations, e.g. the theoretical and experimental works [4–10]. These investigators have documented the presence of secondary flow due to the Coriolis-induced force. Studies on forced convection heat transfer in rotating ducts have also been carried out [11–18]. Recently, developing forced convection in the entrance region of rotating semiporous-walled ducts [19] has been investigated. In the above studies, the buoyancy effects induced by the centrifugal force were all ignored.

After the advocation of the centrifugal buoyancy effect in radially rotating channels by Morris and Ayhan [20], many investigators have devoted study towards the effects of the centrifugal buoyancy. Theoretically, a perturbation analysis was performed by Siegel [21] to investigate the rotation-induced buoyancy effect on fully-developed flow and heat transfer in a rotating pipe. Soong and Hwang [22, 23] performed similarity analyses on the mixed convection in rotating flat-channel with/without transpiration. As for the experimental studies, Morris and Ayhan's works [20, 24] provided experimental evidence about the significance of rotation-induced buoyancy effects. For the triangular duct, Clifford *et al.* [25] measured the heat transfer performance. The buoyancy effects on both radially outward and inward main flows were considered in some investigations [26–30]. Soong *et al.* [31], by changing the wall-heating temperature, explored the centrifugal buoyancy in a square duct for various through-flow Reynolds numbers. Recently, Han and Zhang [3] studied effect of uneven wall-temperature on local heat transfer.

NOMENCLATURE

a, b	width and height of a rectangular duct, respectively [m]
D_e	equivalent hydraulic diameter, $2ab/(a+b) = 2a/(1+\gamma)$
f	friction factor, $2\bar{\tau}_w/(\rho\bar{w}^2)$
fRe	peripherally averaged friction parameter
$(fRe)_x$	local average of fRe
Gr_Ω	rotational Grashof number, $(\Omega^2 D_e)\beta(T_w - T_0)D_e^3/\nu^2$
$\bar{h}$	peripherally averaged heat transfer coefficient [W m^{-2} °C^{-1}]
h_x	locally averaged heat transfer coefficient [W m^{-2} °C^{-1}]
L	duct length
m	mth iteration
n	dimensionless direction coordinate normal to the duct wall
Nu	peripherally averaged Nusselt number, $\bar{h}D_e/k$
Nu_x	local average of Nu, h_xD_e/k
P'	perturbation term about the mean pressure $\bar{P}$
$\bar{P}, \bar{p}$	dimensionless and dimensional cross-sectional mean pressure
p_m	pressure departure from the reference state [kPa]
Pr	Prandtl number, ν/α
Re	Reynolds number, $\bar{w}D_e/\nu$
Re_Ω	rotational Reynolds number, $\Omega D_e^2/\nu$
Ro	rotation number, $\Omega D_e/\bar{w}$
T	temperature [°C]
u, v, w	velocity components in x, y and z directions, respectively [m s^{-1}]
U, V, W	dimensionless velocity components in X, Y and Z directions, respectively
x, y, z	rectangular coordinate [m]
X, Y, Z	dimensionless rectangular coordinate, $X = x/D_e$, $Y = y/D_e$, $Z = z/D_e$
Z_0, z_0	dimensionless and dimensional distance from rotational axis to inlet, respectively.

Greek symbols

α	thermal diffusivity [m^2 s^{-1}]
β	coefficient of thermal expansion
γ	aspect-ratio of the rectangular duct, a/b
θ	dimensionless temperature, $(T-T_0)/(T_w-T_0)$
ν	kinematic viscosity [m^2 s^{-1}]
ξ	dimensionless vorticity in axial direction
ρ	density [kg m^{-3}]
τ_w	wall shear stress [kPa]
Ω	angular velocity of rotation [s^{-1}].

Subscripts

b	bulk fluid quantity
o	condition at inlet
w	value at wall.

Superscript

–	averaged value.

However, due to different test models, conditions, and measurement techniques, there are noticeable inconsistencies between the data by various groups. Furthermore, for sufficiently high rotation rates, the rotating models in laboratory work have to be small in size, for which the difficulty in detailed flow measurement is inevitable. In this situation, numerical simulation can play a complementary role and provide the details of the local flow characteristics. Recently, developing laminar flow and heat transfer through rotating channels were studied extensively by using the finite-difference method [32, 33], whereas the buoyancy effect was not discussed in detail. For a turbulent through-flow, Prakash and Zerkle [34] studied the heat transfer performance with consideration of density variation (or buoyancy effects); however, the local flow development and the evolution of the secondary vortices were not emphasized. Strictly speaking, a discussion on mixed convection in radially rotating rectangular ducts in a view of detailed local flow solutions has not been reported yet.

In practical applications, the rectangular ducts are more appropriate than triangular or circular ducts for the central portion of the cooling passage in the turbine blade, and the flow typically remains developing for almost the full length of the duct. Additionally, in radially rotating systems, rotation-induced buoyancy effects could be significant and should be considered. Detailed flow structure and heat transfer mechanisms under the influences of Coriolis and centrifugal buoyancy effects are of academic interest, while the friction factors and heat transfer rates are of importance in practical applications. These reasons motivate the present study which treats the flow and thermal characteristics in radially oriented rotating rectangular ducts with consideration of the rotation-induced buoyancy effects. A numerical procedure is developed to solve the vorticity–velocity formulation of the parabolic–elliptic governing equations for the present three-dimensional developing mixed convection problem.

ANALYSIS

Consider the coolant air flows through an isothermally-heated radially rotating rectangular duct as

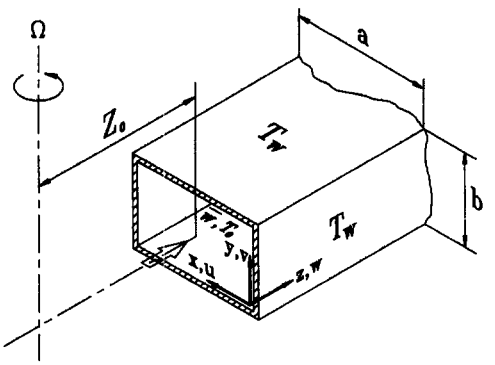

Fig. 1. Schematic diagram of the physical system.

shown in Fig. 1. The cartesian coordinate $Oxyz$ is fixed on the inlet and rotates with the duct. The u, v and w are the velocity components in the x, y and z directions, respectively. A uniform axial velocity $\bar{w}$ and constant inlet temperature T_0 are imposed at the entrance $z = 0$. The distance between the inlet plane and the rotating axis is denoted by z_0. To facilitate the analysis, the flow is assumed to be steady, laminar, and of constant properties, and the stress work effects are ignored. Gravitational force is neglected for its small magnitude compared to the rotation-induced centrifugal force. The Boussinesq approximation and a linear density–temperature relation, $\rho = \rho_0[1-\beta(T-T_0)]$ with ρ_0 as the density evaluated at the reference temperature T_0, are invoked for the consideration of centrifugal-buoyancy.

Vorticity–velocity formulation

The pressure gradient and centrifugal force terms in the x- and z-directions are $-\partial p/\partial x+\rho\Omega^2 x$ and $-\partial p/\partial z+\rho\Omega^2(z_0+z)$, respectively. By defining a pressure function p_m and $p_m = p-p_0$, where p_0 denotes the flow pressure at the inlet, and rearranging the pressure and centrifugal force terms, one has:

$$-\partial p/\partial x+\rho\Omega^2 x = -\partial p_m/\partial x-\rho\beta(T-T_0)\Omega^2 x \quad (1a)$$

$$-\partial p/\partial z+\rho\Omega^2(z_0+z) = -\partial p_m/\partial z-\rho\beta(T-T_0)\Omega^2(z+z_0). \quad (1b)$$

For convenience in implementing the axial marching integration, the pressure function $p_m(x,y,z)$ is split into a cross-sectional average $\bar{p}(z)$ driving the main flow and a perturbation portion $p'(x,y)$ driving the cross stream flow, viz.

$$p_m = \bar{p}(z)+p'(x,y). \quad (2)$$

Together with the assumptions of negligibly small axial momentum and heat diffusion, this 'pressure uncoupling' follows the parabolic-flow practice and permits a marching-integration procedure [17, 35].

Considering the above pressure splitting and perform a proper scaling procedure, the dimensionless form of the continuity, momentum and energy equations can be written as

$$\partial U/\partial X+\partial V/\partial Y+\partial W/\partial Z = 0 \quad (3)$$

$$U\partial U/\partial X+V\partial U/\partial Y+W\partial U/\partial Z+2Ro\,W = -\partial P'/\partial X-Gr_\Omega/Re^2\,\theta X+(\partial^2 U/\partial X^2+\partial^2 U/\partial Y^2)/Re \quad (4)$$

$$U\partial V/\partial X+V\partial V/\partial Y+W\partial V/\partial Z = -\partial P'/\partial Y+(\partial^2 V/\partial X^2+\partial^2 V/\partial Y^2)/Re \quad (5)$$

$$U\partial W/\partial X+V\partial W/\partial Y+W\partial W/\partial Z = -\mathrm{d}\bar{P}/\mathrm{d}Z-(Gr_\Omega/Re^2)\theta(Z_0+Z)+(\partial^2 W/\partial X^2+\partial^2 W/\partial Y^2)/Re+2Ro\,U \quad (6)$$

$$U\partial\theta/\partial X+V\partial\theta/\partial Y+W\partial\theta/\partial Z = (\partial^2\theta/\partial X^2+\partial^2\theta/\partial Y^2)/(Pr\,Re). \quad (7)$$

By performing the cross-differentiation of equations (4) and (5) to eliminate the pressure terms, and using a dimensionless axial vorticity function, $\xi = \partial U/\partial Y-\partial V/\partial X$, one has the axial vorticity transport equation:

$$U\partial\xi/\partial X+V\partial\xi/\partial Y+W\partial\xi/\partial Z+\xi(\partial U/\partial X+\partial V/\partial Y)+(\partial W/\partial Y\cdot\partial U/\partial Z-\partial W/\partial X\cdot\partial V/\partial Z)+2Ro\,\partial W/\partial Y = (\partial^2\xi/\partial X^2+\partial^2\xi/\partial Y^2)/Re-(Gr_\Omega/Re^2)X\partial\theta/\partial Y. \quad (8)$$

The equations of the transverse velocity components (U, V) can be derived from the continuity, equation (3), and the definition of axial vorticity:

$$\partial^2 U/\partial X^2+\partial^2 U/\partial Y^2 = \partial\xi/\partial Y-\partial^2 W/\partial X\,\partial Z \quad (9)$$

$$\partial^2 V/\partial X^2+\partial^2 V/\partial Y^2 = -\partial\xi/\partial X-\partial^2 W/\partial Y\,\partial Z. \quad (10)$$

The overall mass flow rate at every axial location must be balanced by satisfying

$$\int_0^{(1+\gamma)/(2\gamma)}\int_0^{(1+\gamma)/2} W\,\mathrm{d}X\,\mathrm{d}Y = (1+\gamma)^2/(4\gamma)' \quad (11)$$

and this equation can be used to deduce the axial pressure gradient in equation (6).

In summary, the governing equations consist of the axial momentum equation (6), the axial vorticity equation (8), the transverse velocity components, equation (9) and (10), and the thermal energy equation (7). This formulation is called the velocity–vorticity method [36] and is parabolic–elliptic in nature. The boundary conditions for this problem are given by:

$$U = V = W = 0 \quad \theta = 1 \quad \text{at the duct walls} \quad (12a)$$

$$W = 1 \quad U = V = \xi = \theta = 0 \quad \text{at the entrance } (Z = 0). \quad (12b)$$

Following the usual definitions, the peripheral averages of friction parameter, $f\,Re$, and Nusselt number,

Nu, can be expressed based on the axial velocity and temperature gradients on the duct walls, viz.

$$f\,Re = 2(\overline{\partial W/\partial n})_w \tag{13}$$

$$Nu = -(\overline{\partial\theta_w/\partial n})/(1-\theta_b) \tag{14}$$

where the overbar means the peripheral average and n denotes the dimensionless coordinate normal to the duct wall. The bulk temperature θ_b is defined as

$$\theta_b = \int_0^{(1+\gamma)/(2\gamma)} \int_0^{(1+\gamma)/2} \theta W \,dX\,dY/[(1+\gamma)^2/(4\gamma)]. \tag{15}$$

Governing parameters

There are two geometry parameters, Z_0 and γ, and four flow/thermal parameters, Re, Ro, Gr_Ω, and Pr, involved in the problem. To reduce the computational efforts, the dimensionless distance from the inlet plane to the axis of rotation is set to be zero, $Z_0 = 0$, and the Prandtl number $Pr = 0.7$ for air is used in the computations. Effects of the rest are investigated. The rotation number Ro characterizes the Coriolis effect or the relative significance of the Coriolis-induced secondary flow to the forced flow effects. The rotational Grashof number Gr_Ω measures the importance of the rotation-induced buoyancy effects. The cross-sectional aspect-ratio, γ, is the major geometry parameter considered in the work. The flow characteristics, especially the evolution of the secondary vortices, may be significantly influenced by the change in aspect-ratio. In the present study, the rotation number, Ro, ranges from 0 to 0.1, the rotational Grashof number, Gr_Ω, lies between -2×10^4 and 2×10^4, the range of the Reynolds numbers considered is $500 \leqslant Re \leqslant 2000$, and the ducts of $\gamma = 0.5$, 1, and 2 are investigated.

METHOD OF SOLUTION

The vorticity–velocity method for three-dimensional parabolic flow [36, 37] is employed for solution of the present problem, in which the equations for the unknowns U, V, W, ξ, θ and $d\bar{P}/dZ$ are coupled. A marching technique based on the DuFort–Frankel scheme [19, 38] is developed for the solution of equations (6)–(10). The solution procedure is briefly stated as follows and the details can be referred to ref. [19]. For any axial location, with the known values of U, V and assigned $(d\bar{P}/dZ)$, the axial velocity W at the current position is obtained from equation (6), with the constraint of global continuity (11), to meet the requirement of constant flow rate. With the known values of U, V and W, the equations (7), and (8) for θ and ξ subjected to the boundary conditions can be solved by the DuFort–Frankel method. The elliptic-type equations (9) and (10) are then solved for U and V by iteration. The boundary vorticity can be evaluated by using the expression proposed in equation [37]. At each axial location, iteration is performed until the specified stopping criterion, viz.

$$\varepsilon = \mathrm{Max}\,|\phi_{i,j}^{m+1} - \phi_{i,j}^{m}|/\mathrm{Max}\,|\phi_{i,j}^{m+1}| < 10^{-5} \tag{16}$$

is satisfied. In equation (16), ϕ may stand for U or V, m is the number of iteration. The above solution procedure is repeated at each cross plane from the inlet to the downstream axial location of interest.

The grid-dependence test was performed before the main course of the computations. The grids were arranged to be uniform in the cross-sectional plane but non-uniformly distributed in the axial direction for the uneven variations of field properties in the entrance region. The results reveal that the deviations in Nu and $f\,Re$ calculated with I (X-dir.) $\times$ J (Y-dir.) $= 35\times35$ and 45×45 ($\Delta Z = 0.01$–0.05) are always less than 3%. Furthermore, the deviations in Nu and $f\,Re$ calculated on the grids of $I\times J(\Delta Z) = 35\times35$ (0.002–0.05) and 35×35 (0.01–0.05) are all less than 1%. Accordingly, the computations on the grid of $I\times J(\Delta Z) = 35\times35$ (0.01–0.05) are considered to be sufficiently accurate. The computations through the study are all performed on the latter grid system.

RESULTS AND DISCUSSION

Comparisons with the previous results

As a partial verification of the computational procedure, the results were initially obtained for convection heat transfer in a radially oriented rotating rectangular duct with centrifugal buoyancy effect. Figure 2 shows the comparisons of the predicted results with the numerical results [33] and experimental data [31]. The present computations were performed for the same flow configuration and at the same conditions that shown in the experiment [31]. Further, the buoyancy effect in each case was considered and the calculations of the Nusselt number followed the same definition as that in ref. [31]. The present predictions appear slightly higher than the predictions in ref. [33] for the difference in axial distance Z_0 (shown in Fig. 2). The numerical results in two studies agree well, but both of them under-predict the measured data and the deviation enhances with increasing Reyn-

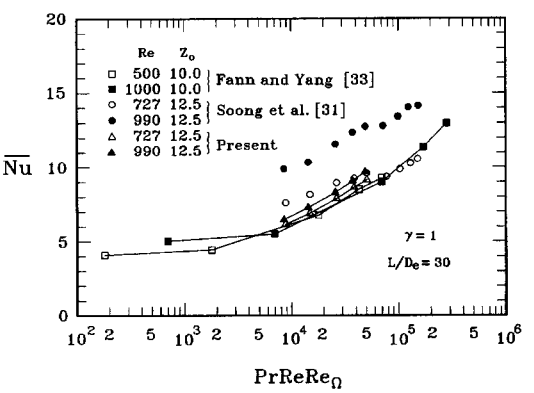

Fig. 2. Comparisons of the present vorticity–velocity solutions with the previous numerical and experimental data.

olds number. It is attributed to the uncertainties in initial swirl and the turbulence level involved in the experiments. Generally speaking, however, the present predictions are in reasonable agreement with the previous predictions [33].

Evolution of secondary vortices

Figure 3(a)–(c) depicts axial evolution of the cross-flow at $Re = 1500$ in a square duct ($\gamma = 1$) with rotational parameters $(Ro, Gr_\Omega) = (0.05, 1 \times 10^4)$, $(0.1, 1 \times 10^4)$, and $(0.05, -2 \times 10^4)$, respectively. Each vector is composed of the velocity components in the x- and y-directions. In Fig. 3(a), near the entrance the flow develops as a boundary layer type one, where all the velocity vectors are directed toward the center of the duct, see the cross-flow at $Z = 0.208$. As the fluid moves downstream, the rotational effects become important. A pair of counter-rotating primary vortices are induced and circulate from the trailing ($X = 0$) to leading ($X = 1$) walls along the side walls ($Y = 0$ and 1) and return from the leading to trailing walls through the central core of the flow ($Y = 0.5$). The letters T and L in all figures denote trailing and leading walls, respectively. The vortex-pair continuously evolves downstream and a relatively weak second vortex-pair forms near the trailing wall at $Z = 36.02$ in Fig 3(a). At $Z = 40.00$, an another weak vortex-pair emerges near the corners as the third one.

Coriolis effects on the secondary flow pattern can be illustrated by changing the rotation number to a value of $Ro = 0.1$ based on the case in Fig. 3(a). Comparison of the corresponding cross-flow patterns in Fig. 3(a) and (b) reveals that, for the large Coriolis effects in the latter, the vortex cores migrate toward the side walls, accelerating the flows along the side walls and decelerating the flow in the core region. As the fluid reaches certain axial location, e.g. $Z = 22.52$, a second pair of vertices emerges near the corners of the trailing wall. As the flow marches downstream, the second (near the corners) pair of vortices decay and is wiped out by the primary vortices. Further downstream, a pair of small counter-rotating vortices is found near the centerline of the trailing wall, as the cross-flow at $Z = 27.54$ shown in Fig. 3(b). This pair of small vortices grows as the flow moves in the axial direction.

To explore the thermal effect on the vortex evolution, results of a buoyancy-assisted flow of $Gr_\Omega = -2 \times 10^4$ are plotted in Fig. 3(c) and compared with the buoyancy-opposed solutions of $Gr_\Omega = 1 \times 10^4$ in Fig. 3(a). Relatively, the buoyancy-assisting effect enhances the strength of the primary vortices as well as changing the position of the vortex cores.

The same phenomenon can be found for the ducts of various aspect-ratios. Figure 4(a) and (b) shows the cross-flow maps at $Z = 40.00$ under the influences of various buoyancy effects in the rectangular ducts of $\gamma = 0.5$ and 2.0, respectively. By inspecting Figs. 4(a), 4(b), 3(a) and 3(c), it can be found that the primary vortex cores migrate towards to the leading wall as the value of Gr_Ω changes from 2×10^4 to -2×10^4. The buoyancy effects alter the axial velocity distribution, and through the link of the continuity equation, influence the cross-flow.

Figure 5 presents secondary-flow patterns in duct of $\gamma = 0.5$ at high rotation rate, $Ro = 0.1$. Due to the Coriolis force effect, the secondary vortices form near the two side walls. At $z = 22.52$, a tendency of the second pair of vortices appears adjacent to the center of the trailing wall. As the flow moves downstream, the secondary pair of vortices becomes stronger, while the cross-flow pattern still remains symmetric up to the axial location of $z = 31.51$. At $z = 36.02$, the third pair of vortices emerges at the trailing wall and the second pair moves away from the symmetric plane. Eventually, the cross-flow becomes asymmetric in this situation of the high Coriolis effect. This Coriolis instability phenomenon has also been reported in the previous studies [17, 39].

Axial velocity and temperature distributions

The developing axial velocity profiles along the centerline $Y = 0.5$ at various axial locations are shown in Fig. 6. For the case of $Re = 1500$, $Ro = 0.05$ and $Gr_\Omega = 1 \times 10^4$ in Fig. 6(a), near the entrance, the velocity profile (curve A) is fairly uniform over the cross-section. As the flow develops (curves B and C), the velocity in the core region is accelerated due to the entrance effect. Further downstream, the velocity profile becomes distorted with the velocity peak moving toward the trailing wall due to the secondary flow effect. Finally, at $Z = 40.00$, the velocity profile forms a skewed parabolic shape. It is also noted in Fig. 6(a) that the axial velocity gradient and, therefore, the skin friction on the trailing wall is larger than that on the leading wall.

Comparing the cross-flow maps at $Z = 4.51$ and $Z = 15.03$ in Fig. 3(a), it is found that the velocity vectors at the centerline $Y = 0.5$, where $V = 0$ and $\partial V/\partial Y = 0$, change remarkably in the X-direction, i.e. large values of $\partial U/\partial X$. From continuity, one has $\partial W/\partial Z = \partial U/\partial X$ at $Y = 0.5$: therefore, large $\partial U/\partial X$ implies large axial velocity gradient, $\partial W/\partial Z$. Also, from the cross-flow maps in Fig. 3(a), the center line ($Y = 0.5$) velocity vectors in the regions of $22.52 \leqslant Z \leqslant 40.00$ present no significant change near the leading wall ($X = 1.0$) and only slight changes near the trailing wall ($X = 0$) due to evolution of the secondary vortices. These are the reasons why the velocity distributions at $Z \geqslant 15.03$ are so different from the upstream ones and why the curves D, E and F present a very similar shape in Fig. 6(a).

Figure 6(b) gives the axial velocity profiles at $Y = 0.5$ for $Ro = 0.1$, $Gr_\Omega = 1 \times 10^4$, and $\gamma = 1$. As above, curves A–C show the developing velocities in the entrance region. At $Z = 15.03$ (curve D), the axial velocity is distorted and shows a similar trend to that in Fig. 6(a). Further downstream, the axial velocity peak moves toward the trailing wall ($X = 0$) as shown in curves E–G. This is clearly due to the onset of

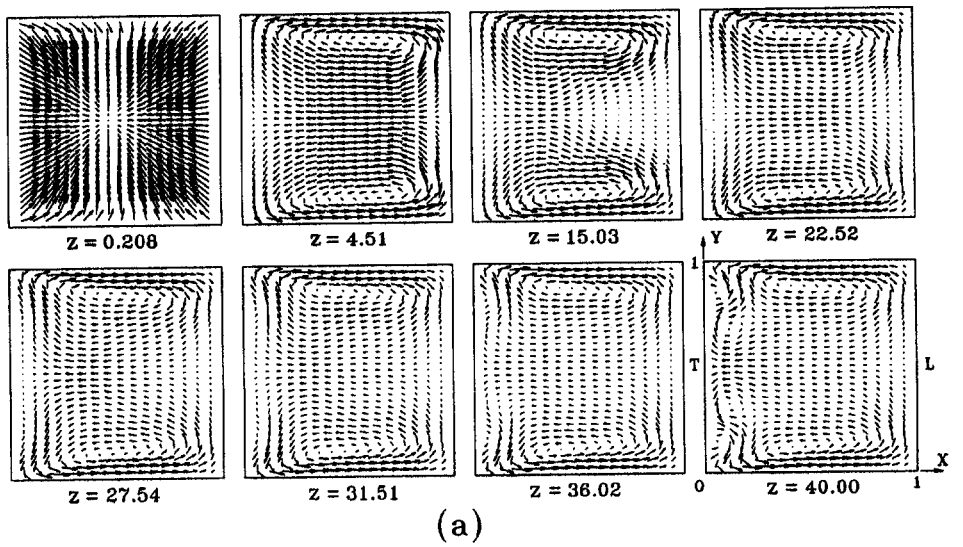

(a)

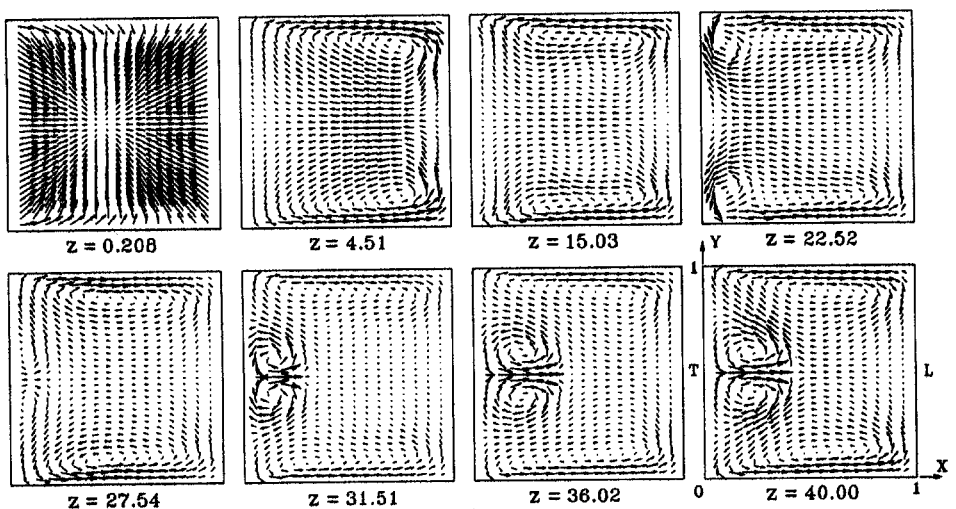

(b)

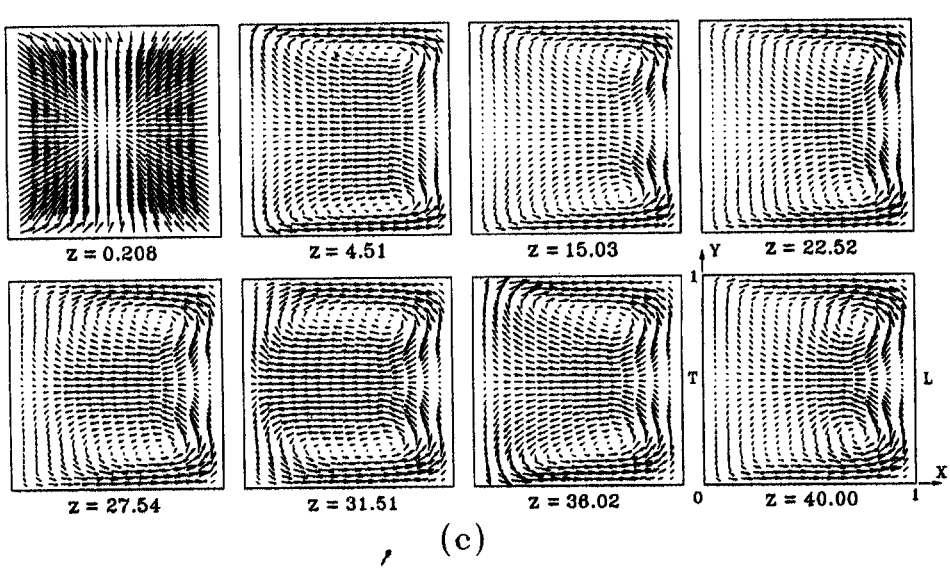

(c)

Fig. 3. Secondary flow maps in a square duct for $Re = 1500$ and (a) $Ro = 0.05$, $Gr_\Omega = 1 \times 10^4$, (b) $Ro = 0.10$, $Gr_\Omega = 1 \times 10^4$, and (c) $Ro = 0.05$, $Gr_\Omega = -2 \times 10^4$.

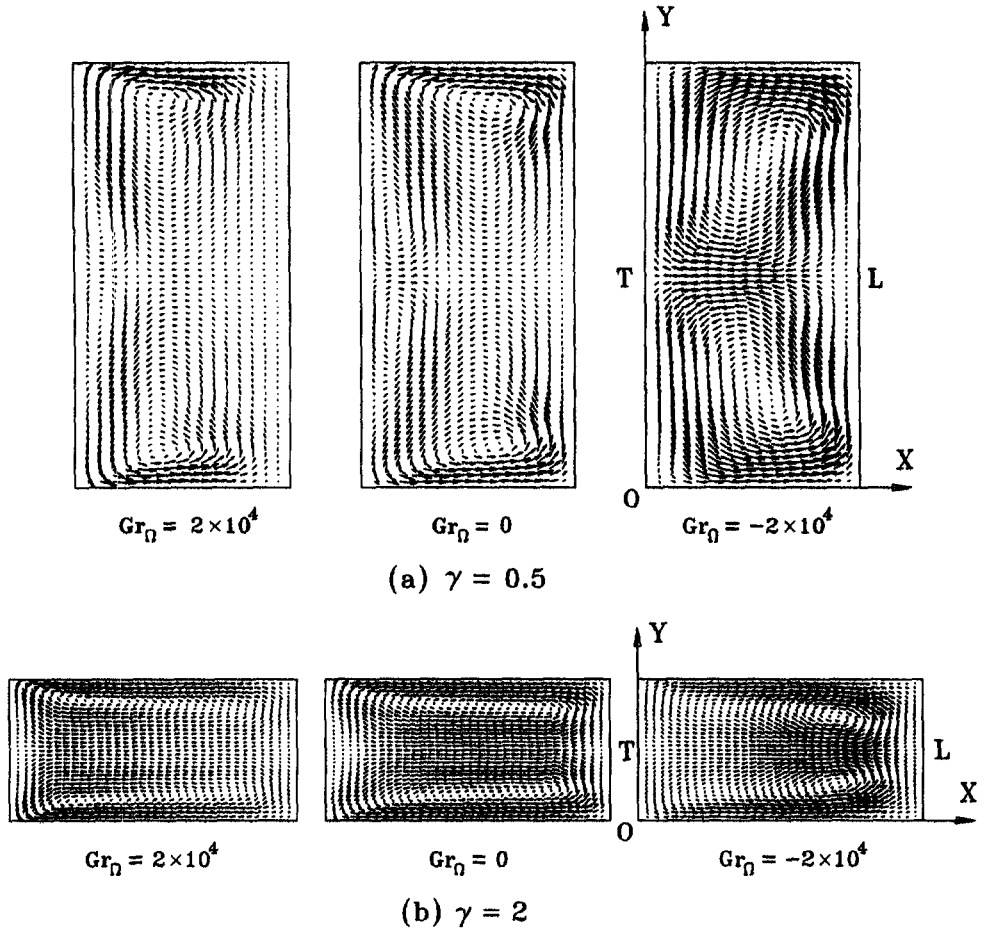

Fig. 4. Centrifugal buoyancy effects on cross-flow at $Z = 40.00$ for $Re = 1500$ and $Ro = 0.05$ in ducts of: (a) $\gamma = 0.5$ and (b) $\gamma = 2.0$.

second pair of counter-rotating vortices near the trailing wall.

In the case of $Gr_\Omega = -2 \times 10^4$ shown in Fig. 6(c), as compared with Fig. 6(a), the higher axial velocity appears near the downstream leading wall ($X = 1$) due to the buoyancy-assisting effect there. Therefore, to satisfy the global continuity, the velocity peak reduces and moves off the trailing wall ($X = 0$).

In a typical case of square duct with $Ro = 0.05$ and $Gr_\Omega = 1 \times 10^4$, Fig. 7(a) shows the temperature distributions in the X-direction in the plane of $Y = 0.5$. The temperature peaks lean toward the trailing wall ($X = 0.0$) and the temperature gradients are more pronounced than that at the leading wall ($X = 1.0$), especially at the downstream locations where the strong secondary vortices emerge. In the plane of $X = 0.5$, see Fig. 7(b), the temperature distributions are symmetric with respect to $Y = 0.5$, corresponding to the symmetric flow pattern in the cross plane.

Buoyancy effects are always closely related to the temperature fields of the fluid flow. Temperature distributions on the planes of $Y = 0.5$ and $X = 0.5$ for a buoyancy-opposed flow at $Re = 1500$, $Ro = 0.05$ and $Gr_\Omega = 1 \times 10^4$ are shown in Fig. 7(a) and (b). To explore the influences of centrifugal buoyancy, the θ-distributions on the plane of $Y = 0.5$ for the corresponding buoyancy-free case ($Gr_\Omega = 0$) and a buoyancy-assisting one ($Gr_\Omega = -2 \times 10^4$) are plotted as Fig. 7(c) and (d). In Fig. 7(b), it is seen that the θ-distributions are symmetric with respect to the plane of $Y = 0.5$. Compared with the buoyancy-free results in Fig. 7(c), the counter-buoyancy effect of $Gr_\Omega > 0$ in Fig. 7(a) tends to sharpen the temperature curves at the trailing wall. However, for $Gr_\Omega = -2 \times 10^4$ in Fig. 7(d), centrifugal buoyancy effects on temperature distributions can be clearly shown in the downstream portion of the duct, e.g. at $Z = 31.51$ and 40.00, where the stronger centrifugal force appears. Examining θ-curves at $Z = 40.00$ in Fig. 7(a), (c) and (d), the temperature distribution for $Gr_\Omega = -2 \times 10^4$ is flatter than that for the other two cases. The temperature gradient, as well as the heat transfer rate, at the trailing wall is relatively small, while that at the leading wall is relatively large for $Gr_\Omega = -2 \times 10^4$ as compared with the results for $Gr_\Omega = 0$ and 1×10^4.

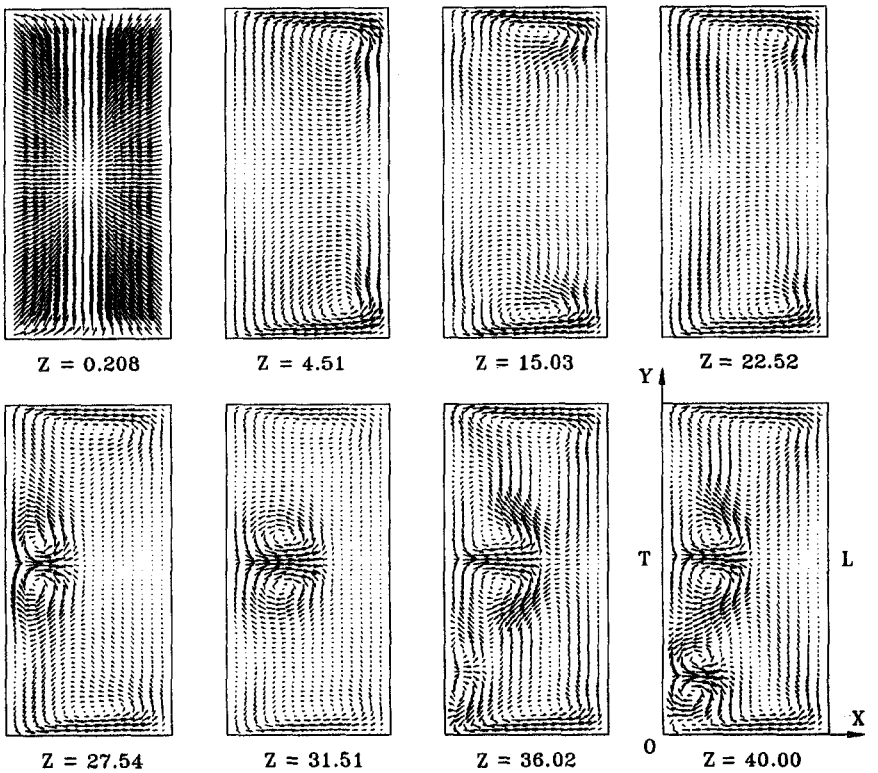

Fig. 5. Evolution of the asymmetric secondary vortices in duct of $\gamma = 0.5$ for $Re = 1500$, $Ro = 0.10$, $Gr_\Omega = 1 \times 10^4$.

Coriolis effects on friction factors and heat transfer rates

In Fig. 8, the axial variations of the peripheral averages, $f\,Re$ and Nu; the trailing wall, leading wall and the side wall friction factors, $(f\,Re)_x$, and Nusselt numbers, Nu_x, with the rotation number as a parameter are plotted. It is clear that the rotational effects are negligible up to a certain entry length Z. This axial distance depends primarily on the magnitude of the rotation number Ro. The greater the Ro, the shorter the unaffected distance. In Fig. 8(a), each curve branches out from the curve for purely forced convection (i.e. $Ro = 0$), and, after reaching a local minimum value, the curve goes up. The occurrence of the first minimum in $f\,Re$ and Nu is due to the appearance of the primary vortex pair. It is worth noting that, for $Ro = 0.075$ and 0.1, oscillations in the variations of $f\,Re$ and Nu exist after the first local minimum. This behavior is related to the emergence and decay of the second pair of vortices near the trailing wall. In addition, larger $f\,Re$ and Nu result for a larger Ro due to the stronger Coriolis force.

The variations of locally averaged $f\,Re$ and Nu on the trailing and leading walls are of interest. Figure 8(b) shows the effects of the rotation number Ro on the $f\,Re$ and Nu on the trailing and leading walls for $Gr_\Omega = 1 \times 10^4$, $Re = 1500$ and $\gamma = 1$. Near the entrance, the $f\,Re$ and Nu on the leading wall fall steeply. As flow moves downstream, $f\,Re$ and Nu gradually decrease and then level off. Furthermore, in the Ro range considered, the changes in $f\,Re$ and Nu on the leading wall are relatively small as compared with the Ro-dependence of $f\,Re$ and Nu on the trailing wall. The values of $f\,Re$ and Nu on the trailing wall vary significantly with Ro. At low Ro (e.g. $Ro = 0.025$), a sharp decrease in $f\,Re$ and Nu is followed by a moderate recovery. As Ro is increased to $Ro = 0.075$, the curves of $f\,Re$ and Nu become oscillatory for $Z > 20$. The number and the amplitude of this kind of oscillation have a tendency to increase with Ro. These behaviors result from the generation and disappearance of multiple pairs of vortices on the trailing wall and their complex interaction, see e.g. Fig. 3. Additionally, the local maximum moves upstream as Ro increases, which implies that a premature Coriolis instability can be expected for high Ro.

Figure 8(c) reveals the locally averaged friction factor and heat transfer coefficient on the side walls. Due to the symmetric flow in this case the boundary parameters, $f\,Re$ and Nu, for the two side walls are the same. Comparing the results in Fig. 8(c) with 8(b), it is found that the $f\,Re$ and Nu on the side walls appear higher than those on the leading wall but somewhat lower than those on the trailing wall. In addition, oscillatory phenomena in $f\,Re$ and Nu are also found on the side walls for the curves of $Ro = 0.5$, 0.075 and 0.1. It is worth noting that the axial position of the local minimum on the side wall in the curves of

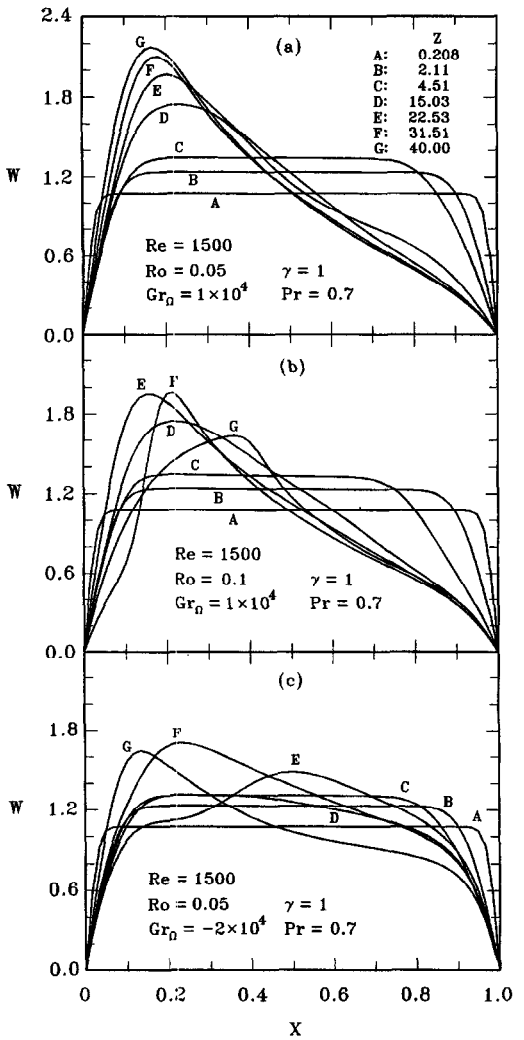

Fig. 6. Rotational effects on developments of axial velocity profiles at $Y = 0.5$: (a) $Ro = 0.05$, $Gr_\Omega = 1 \times 10^4$; (b) $Ro = 0.1$, $Gr_\Omega = 1 \times 10^4$; (c) $Ro = 0.05$, $Gr_\Omega = -2 \times 10^4$.

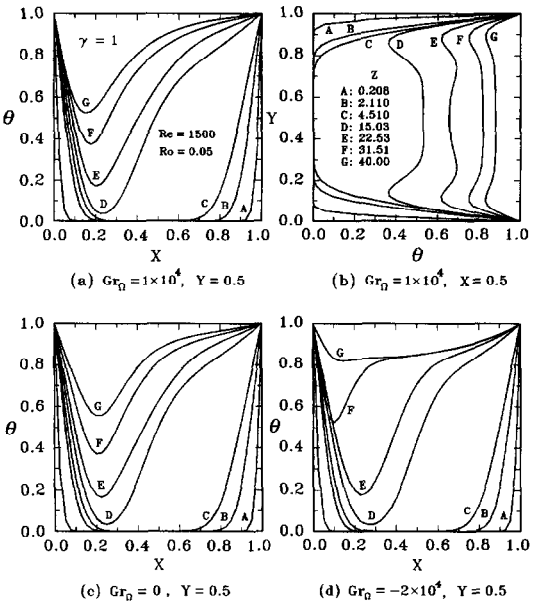

Fig. 7. Flow temperature distributions in a square duct for $Re = 1500$, $Ro = 0.05$; (a) $Gr_\Omega = 1 \times 10^4$, $Y = 0.5$; (b) $Gr_\Omega = 1 \times 10^4$, $X = 0.5$; (c) $Gr_\Omega = 0$, $Y = 0.5$; and (c) $Gr_\Omega = -2 \times 10^4$, $Y = 0.5$.

$Ro = 0.075$ and 0.1 is the same as that of the local maximum on the trailing wall. This is caused by the emergence of a small pair of vortices near the trailing wall, which diminishes the strength of the principal pair of vortices and, as a result, reduces the $f\,Re$ and Nu on the side walls. After the generation of the small vortex, the small vortex decays and is wiped out by the principal vortex.

Centrifugal buoyancy effects on friction factors and heat transfer rates

In a high rotation rate and/or a high wall-to-coolant temperature difference in rotating elements, the centrifugal force may play a very critical role in the flow and heat transfer mechanisms. Hence, it is interesting to examine the effect or centrifugal buoyancy on the flow and heat transfer. Figure 9(a) shows the effects of centrifugal buoyancy on the $f\,Re$ and Nu for $Ro = 0.05$, $Re = 1500$ and $\gamma = 1$. For $Gr_\Omega < 0$, the buoyancy-assisting effects enhance the heat transfer rates, and the extent of enhancement in heat transfer increases with the magnitude of Gr_Ω. Note that the Nu-curve for $Gr_\Omega = -2 \times 10^4$ drops drastically at $Z = 32$. The axial evolution of the fluid temperature in Fig. 7(d) gives a clue for the Nu-variation. This reduction in heat transfer rate is attributed to the uniformity tendency and the rapid change in θ-distribution in the region of $Z > 30$. The effects of the centrifugal buoyancy force on the $f\,Re$ are relatively more complicated. Conversely, in a buoyancy-opposed flow with $Gr_\Omega > 0$, the axial variation of the heat transfer rate is reduced.

For $Z < 15$ in Fig. 9(a), a larger $f\,Re$ is noted for a buoyancy-assisted flow ($Gr_\Omega < 0$). But for $Z > 15$, the reverse trend can be found. For $Gr_\Omega = -2 \times 10^4$, the uneven variation of $f\,Re$ in the downstream portion is closely related to the axial velocity development presented in Fig. 6(c). It is noteworthy that the buoyancy effects on the velocity field in the present three-dimensional flow are rather different from that in a two-dimensional case for the complexities of the appearance of the secondary vortices in the former. The oscillation in the Nu-curve for $Gr_\Omega = -2 \times 10^4$ is a consequence of migration of the primary vortex core.

Aspect-ratio effects on friction factors and heat transfer rates

The effects of the duct aspect-ratio on the friction factor and Nusselt number are also of interest. The axial variations of $f\,Re$ and Nu with Gr_Ω as a parameter in the ducts of $\gamma = 0.5$ and 2 are shown in Fig. 9(b) and (c), respectively. Comparing the results of Fig. 9(a), (b) and (c) indicates that, within the range of the aspect-ratio under consideration, smaller $f\,Re$

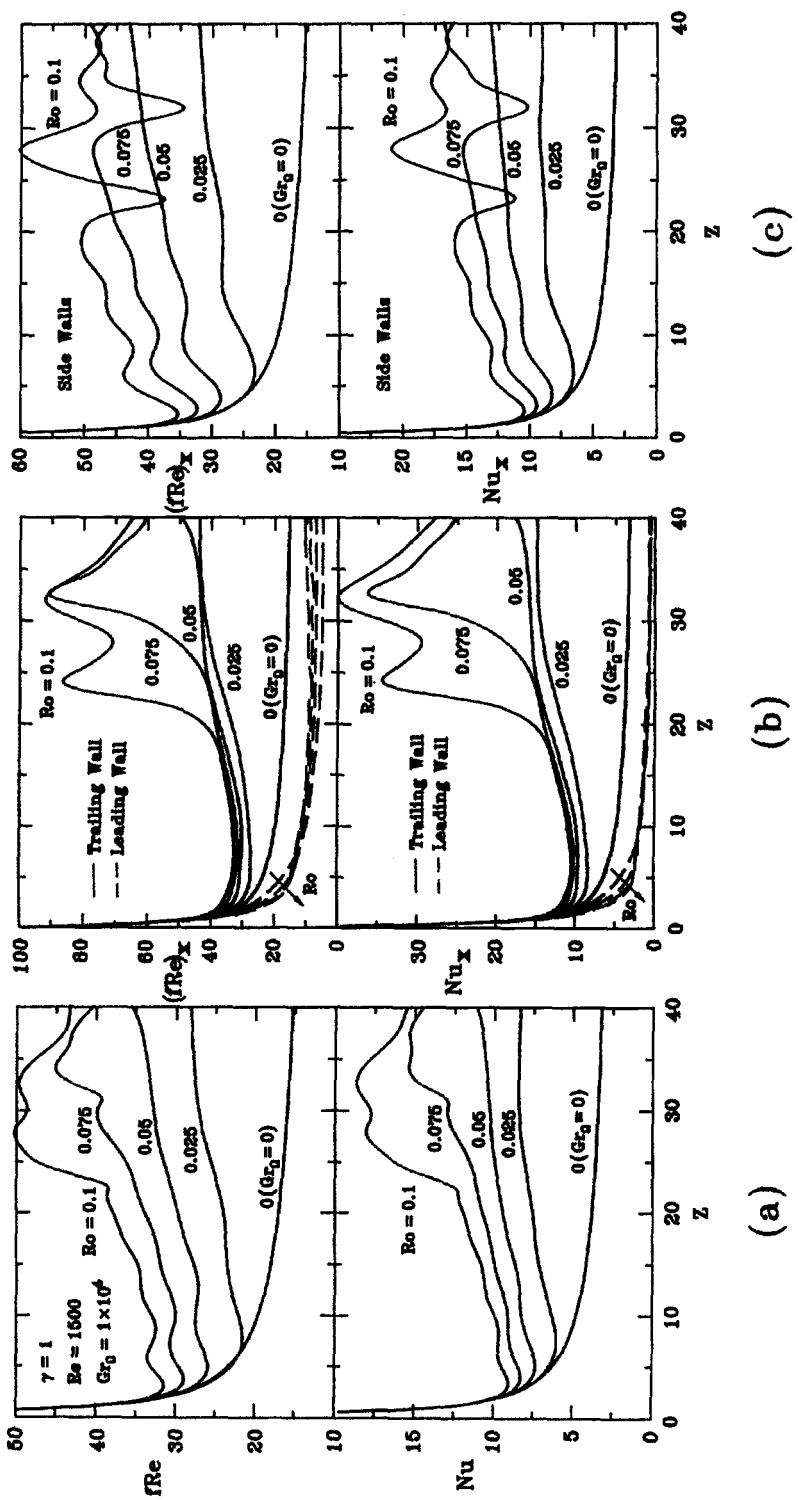

Fig. 8. Coriolis effects on the variations local friction factors and Nusselt numbers of: (a) the peripheral averages of 4 walls; (b) the leading and trailing walls; and (c) side walls.

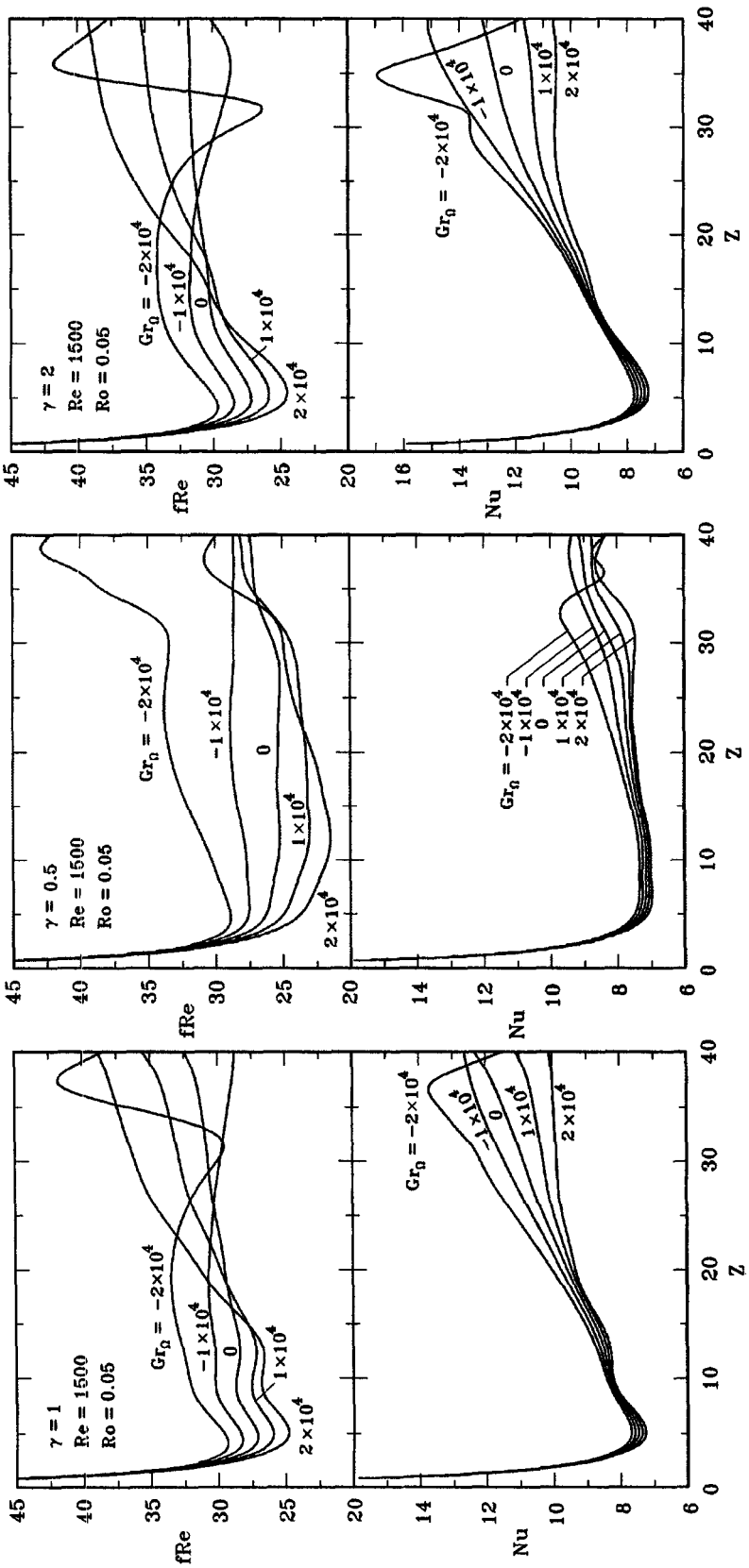

Fig. 9. Centrifugal buoyancy effects on peripheral averages, fRe and Nu, in the ducts of: (a) $\gamma = 1$; (b) $\gamma = 0.5$; and (c) $\gamma = 2$.

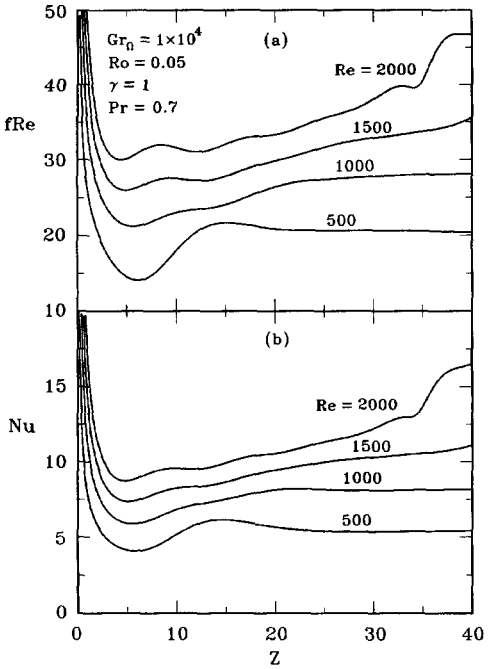

Fig. 10. Forced flow effects on peripheral averages, $f\,Re$ and Nu, in a square duct for $Ro = 0.05$, $Gr_\Omega = 1 \times 10^4$.

and Nu are noted for a system with a smaller aspect-ratio ($\gamma = 0.5$). This is owing to the fact that the relatively weaker secondary motion is presented for aspect ratio $\gamma = 0.5$, which in turn causes a smaller enhancement in $f\,Re$ and Nu.

Reynolds number effects on friction factors and heat transfer rates

Figure 10 shows the Reynolds number effects on the variations of the peripheral averages of the friction factor, $f\,Re$, and the heat transfer rate, Nu, for $Re = 1500$, $Ro = 0.05$, $Gr_\Omega = 1 \times 10^4$ and $\gamma = 1$. As shown in Fig. 10, the large $f\,Re$ and Nu are experienced for a system with a higher Reynolds number due to a large forced-convection effect. It is also found in the separate computation run that the centrifugal buoyancy effect diminishes with the increasing Re.

CONCLUSIONS

The flow and heat transfer characteristics in radially rotating rectangular ducts with consideration of centrifugal buoyancy have been studied numerically. A relatively novel vorticity–velocity method successively solved the three-dimensional parabolic governing equations. The effects of Coriolis force, centrifugal buoyancy and aspect-ratio on the flow and heat transfer mechanisms are investigated in detail by examining the local flow structure and temperature fields. What follows is a brief summary.

1. The variations of the friction factor $f\,Re$ and Nusselt number Nu demonstrate that the total rotational effects of Coriolis and centrifugal buoyancy forces are negligible until the onset of the secondary motion occurs at a certain axial location. The axial distributions of $f\,Re$ and Nu are characterized by a decay near the entrance due to the entrance effect; but the decay is attenuated by the onset of secondary flow. After reaching a first local minimum, local maximums and minimums of $f\,Re$ and Nu may appear, corresponding to the emergence (growth) and disappearance (decay) of the secondary vortices.
2. The Coriolis effect raises the peripherally averaged friction factors and heat transfer rates. An increase in rotation number Ro causes enhancements in $f\,Re$ and Nu on the trailing wall and their fluctuations along the flow, moderate increases in $f\,Re$ and Nu on the side walls and degradation of $f\,Re$ and Nu on the leading wall.
3. Centrifugal buoyancy effects can alter the axial velocity distribution and, through the coupling of continuity, change the cross-flow patterns, including the strength and core position of the secondary vortices.
4. In general, the peripherally averaged Nusselt number Nu are decreased by a counter effect of centrifugal buoyancy ($Gr_\Omega > 0$). Conversely, the Nu can be enhanced in the presence of the buoyancy-assisting effect ($Gr_\Omega < 0$)
5. Smaller $f\,Re$ and Nu are noted for a rectangular duct with a smaller aspect-ratio ($\gamma = 0.5$) due to the relatively weaker secondary flows.
6. A strong forced flow can lead to increases in $f\,Re$ and Nu and weaken the relative importance of the centrifugal buoyancy effects.

Acknowledgement—The financial support of this research by the National Science Council, R.O.C., through the contract NSC 81-0401-E211-502 is greatly appreciated.

REFERENCES

1. W. D. Morris, *Heat Transfer and Fluid Flow in Rotating Coolant Channels*. John Wiley, Chichester (1981).
2. C. Y. Soong and G. J. Hwang, Convective heat transfer in radially rotating coolant channels of turbomachinery, *Proceedings of the Aero. and Astro Conference, AASRC*, Taipei, R.O.C. (December 1990).
3. J. C. Han and Y. M. Zhang, Effect of uneven wall temperature on local heat transfer in a rotating square channel with smooth walls and radial outward flow, *ASME Trans. J. Heat Transfer* **114,** 850–858 (1992).
4. J. E. Hart, Instability and secondary flow in a rotating channel flow, *J. Fluid Mech.* **45,** 341–351 (1971).
5. H. Ito and K. Nanbu, Flow in rotating straight pipes of circular cross-section, *ASME Trans. J. Basic Eng.* **93,** 383–394 (1971).
6. R. E. Wagner and H. R. Velkoff, Measurement of secondary flows in a rotating duct, *ASME Trans. J. Eng. Power* **94,** 261–270 (1972).
7. A. K. Majumdar, V. S. Pratap and D. B. Spalding, Numerical computation of flow in rotating ducts, *ASME Trans. J. Fluid Eng.* **99,** 148–153 (1977).
8. C. G. Speziale, Numerical study of viscous flow in rotating rectangular ducts, *J. Fluid Mech.* **122,** 251–271 (1982).
9. C. G. Speziale and S. Thangam, Numerical study of

secondary flows and roll-cell instabilities in rotating channel flow, *J. Fluid Mech.* **130,** 377–395 (1983).
10. C. G. Speziale, Numerical solution of rotating internal flows, *Lect. Appl. Math.* **22,** 261–289 (1985).
11. Y. Mori, T. Fukada and W. Nakayama, Convective heat transfer in a rotating radial circular pipe (2nd Report), *Int. J. Heat Mass Transfer* **11,** 1807–1824 (1971).
12. V. I. Lokai and A. S. Limanski, Influence of rotation on heat transfer in radial cooling channels of turbine blades, *Izvestiya VUZ. Aviatsionnaya Tekhnika* **18**(3), 69–72 (1975).
13. L. M. Zysina-Molozhen, A. A. Dergach and G. A. Kogan, Experimental investigation of heat transfer in a radially rotating pipe, *Teplofizika sokikh Temperature* **14**(5), 1108–1111 (1976).
14. D. E. Metzger and R. L. Stan, Entry region heat transfer in rotating radial tubes, AIAA Paper No. 77-189, Fifteenth AIAA Aerospace Sciences Meeting, Los Angeles, CA (1977).
15. V. Vidyanidhi, V. V. S. Suryanarayana and R. Chenchu, An analysis of steady fully developed heat transfer in a rotating straight pipe, *ASME Trans. J. Heat Transfer* **99,** 148 (1977).
16. G. J. Hwang and T. C. Jen, Convective heat transfer in rotating isothermal ducts, *Int. J. Heat Mass Transfer* **33,** 1817–1828 (1990).
17. T. C. Jen, A. S. Lavine and G. J. Hwang, Simultaneously developing laminar convection in rotating isothermal square channels, *Int. J. Heat Mass Transfer* **35,** 239–254 (1992).
18. T. C. Jen and A. S. Lavine, Laminar heat transfer and fluid flow in the entrance region of a rotating duct with rectangular cross section: the effect of aspect ratio, *ASME Trans. J. Heat Transfer* **114,** 574–581 (1992).
19. W.-M. Yan, Developing flow and heat transfer in radially rotating rectangular ducts with wall-transpiration effects, *Int. J. Heat Mass Transfer* **37,** 1465–1473 (1994).
20. W. D. Morris and T. Ayhan, Observation on the influence of rotation on heat transfer in the coolant channel of gas turbine rotor blade, *Proc. Inst. Mech. Engrs* **193,** 303–311 (1979).
21. R. Siegel, Analysis of buoyancy effect on fully developed laminar heat transfer in a rotating tube, *ASME Trans J. Heat Transfer* **107,** 338–344 (1985).
22. C. Y. Soong and G. J. Hwang, Laminar mixed convection in a radially rotating semiporous channel, *Int. J. Heat Mass Transfer* **33,** 1805–1816 (1990).
23. C. Y. Soong and G. J. Hwang, Stress work effects on similarity solutions of mixed convection in rotating channels with wall-transpiration, *Int. J. Heat Mass Transfer* **36,** 845–856 (1993).
24. W. D. Morris and T. Ayhan, An experimental study of turbulent heat transfer in the tube which rotates about an orthogonal axis, *Proceedings of the ICHMT Symposium Heat Mass Transfer and Rotational Machinery*, Dubrovnik, Yugoslavia, 30 August–3 September (1982).
25. R. J. Clifford, S. P. Harasgama and W. D. Morris, An experimental study of local and mean heat transfer in a triangular-sectional duct rotating in the orthogonal mode, *ASME Trans. J. Eng. Gas Turbines Power* **106,** 661–667 (1984); also *Int. J. Turbo. Jet Engines* **2,** 93–106 (1985).
26. K. M. Iskakov and V. A. Trushin, The effect of rotation on heat transfer in the radial cooling channels of turbine blades, *Thermal Engng* **32,** 93–96 (1985).
27. S. P. Harasgama and W. D. Morris, The influence of rotation on the heat transfer characteristics of circular, triangular, and square-sectioned coolant passages of gas turbine rotor blades, *ASME Trans. J. Turbomach.* **110,** 44–50 (1988).
28. J. Guidez, Study of the convective heat transfer in a rotating coolant channel, *ASME Trans. J. Turbomach.* **111,** 43–50 (1989).
29. J. H. Wagner, B. V. Johnson and T. J. Hajek, Heat transfer in rotating passages with square smooth walls and radial outward flow, *ASME Trans. J. Turbomach.* **113,** 42–51 (1991).
30. J. H. Wanger, B. V. Johnson and F. C. Kopper, Heat transfer in rotating serpentine passage with smooth walls, *ASME Trans. J. Turbomach.* **113,** 321–330 (1991).
31. C. Y. Soong, S. T. Lin and G. J. Hwang, An experimental study of convective heat transfer in radially rotating rectangular ducts, *ASME Trans. J. Heat Transfer* **113,** 604–611 (1991).
32. S. Fanns, W. J. Yang and S. Mochizuki, Heat and fluid flow at entrance regions of rotating iso-heat flux channels with laminar throughflow, *Int. J. Numer. Meth. Heat Fluid Flow* **2,** 335–358 (1992).
33. S. Fanns and W. J. Yang, Hydrodynamically and thermally developing laminar flow through rotating channel having isothermal walls, *Numer. Heat Transfer* **A 22,** 247–288 (1992).
34. C. Prakash and R. Zerkle, Prediction of turbulent flow and heat transfer in radially rotating square duct, *ASME J. Turbomach.* **114,** 835–846 (1992).
35. F. P. Incropera and J. A. Schutt, Numerical simulation of laminar mixed convection in the entrance region of horizontal rectangular ducts, *Numer. Heat Transfer* **8,** 707–729 (1985).
36. K. Ramakrishna, S. G. Rubin and P. K. Khosla, Laminar natural convection along vertical square ducts, *Numer. Heat Transfer* **5,** 59–79 (1982).
37. F. C. Chou and G. J. Hwang, Vorticity–velocity method for Graetz problem with the effect of natural convection in a horizontal rectangular channel with uniform wall heat flux, *ASME Trans. J. Heat Transfer* **109,** 704–710 (1987).
38. P. J. Roache, *Computational Fluid Dynamics*, pp. 61–64. Reinhold, New York (1971).
39. S. Fann and W. J. Yang, A numerical study of developing radial flow with rotation, *Int. J. Numer. Meth. Heat Fluid Flow* **3,** 187–204 (1993).